Rover Odometry Aided by a Star Tracker

Jonathan D. Gammell, Chi Hay Tong, Peter Berczi, Sean Anderson, and Timothy D. Barfoot
Institute for Aerospace Studies
University of Toronto
Toronto, Ontario, Canada
{jon.gammell, chihay.tong, tim.barfoot}@utoronto.ca, {peter.berczi, sean.anderson}@mail.utoronto.ca

John Enright
Department of Aerospace Engineering
Ryerson University
Toronto, Ontario, Canada
jenright@ryerson.ca

Abstract—This paper develops a practical framework for estimating rover position in full-dark conditions by correcting relative odometric estimates with periodic, absolute-attitude measurements from a star tracker. The framework is validated using just under 2.5 kilometres of field data gathered at the University of Toronto's Koffler Scientific Reserve at Jokers Hill (KSR) comprised of both wheel odometry and lidar-based Visual Odometry (VO). It is shown that for the wheel odometry solution, the final estimate of rover position was within 21 metres of the groundtruth as calculated by a differential GPS receiver, or 0.85% of the total traverse distance. When the star tracker measurements are artificially limited to occurring approximately every 250 metres, the algorithm still performs well, giving a final position error of 75.8 metres or 3.0%. Preliminary results to replace wheel odometry with lidar-based VO for the development a full-dark visual solution are also presented. The lidar-based VO solution is shown to be capable of outperforming wheel odometry, but more work is required to develop methods to handle the variety of terrain conditions encountered.

Figure 1. The ASRL Clearpath Husky A200 equipped with a laser rangefinder, star tracker, and inclinometer.

TABLE OF CONTENTS

1. INTRODUCTION

Accurately estimating the position of rovers in the absence of a Global Positioning System (GPS) is an ongoing challenge in robotics. The additional weight and power limitations of extraterrestrial operations, such as during missions to the Moon or Mars, further complicate this problem. The simplest solution, wheel odometry, is computationally inexpensive and readily available but is prone to wheel slip on loose terrain and during turns, resulting in poor orientation estimates. A common solution has been to supplement wheel odometry with periodic, absolute-orientation measurements.

Volpe [1] augmented wheel odometry with a sun sensor to calculate rover heading and reported a cross-track error of 6% of distance travelled over a 1 kilometre traverse. Bakambu et al. [2] used a fibre-optic gyroscope and an inclinometer to calculate heading and correct the wheel odometry estimates of autonomous mining vehicles through a Kalman Filter. Baumgartner et al. [3] and Balaram [4] discussed adding a sun sensor to inertial navigation sensors and wheel odometry for long-range Martian autonomy. Lamon and Siegwart [5] developed algorithms to fuse inertial navigation systems with wheel odometry and demonstrated their algorithm's ability to traverse 3D obstacles.

Alternatively, missions such as the Mars Exploration Rovers (MERs) and the Mars Science Laboratory (MSL) have employed stereo Visual Odometry (VO) [6] to estimate relative motion in place of wheel odometry. VO does not suffer from wheel slip and is quite accurate over short-to-medium distances even on loose terrain [7]; however, the error grows super-linearly over kilometer-long traverses [8].

As with wheel odometry, previous VO work has focused on incorporating attitude measurements from a sun sensor and an inclinometer to correct for systematic errors [9], [10]. These additional sensors come at a near-negligible extra mass, power, and computational cost to the rover platform while exploiting the existing dependence of the stereo camera on the presence of the sun as a light source. Lambert et al. [11] demonstrated both continuous and periodic corrections from the sun sensor and inclinometer, reporting errors of less than 1% of distance travelled over a 10 kilometre data set.
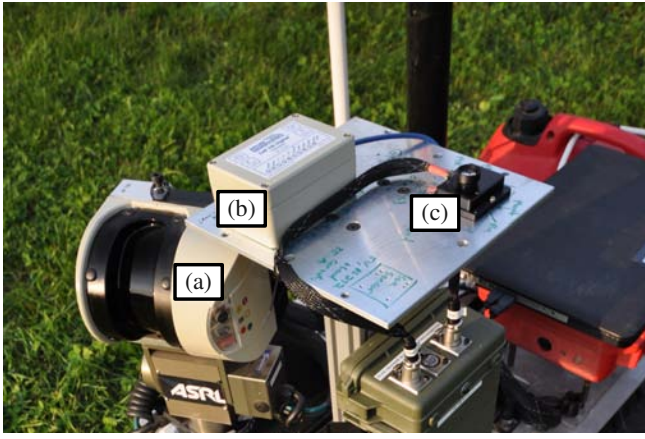
Figure 2. The rover sensor payload with (a) a SICK lidar, (b) an inclinometer, and (c) a Sinclair Interplanetary star tracker.

All these algorithms depend on the sun (sun-sensors) or well-known magnetic fields (digital compasses) for their absolute heading. Recently, there has been an increase in scientific interest around the lunar poles, specifically the South Pole. It is hypothesized that volatiles, such as water ice, may be trapped in permanently shadowed craters [12] and that a rover mission could be used to investigate. The lack of atmosphere, combined with low sun elevation, create an environment at the poles where sensors would be exposed to both direct sun illumination and complete darkness. This is a difficult environment for passive stereo cameras or sun sensors, and the magnetic field is insufficient for digital compasses.

We can address these issues by replacing the stereo camera in VO with lighting-invariant sensors; possible systems include actively-illuminated stereo cameras [13], [14] and lidar for VO [15], [16]. These systems have similar biases and errors as stereo-camera VO, and similarly benefit from absolute-heading corrections.

One system that is analogous to the sun sensor (working in full-dark conditions without relying on magnetic fields) is a star tracker. Star trackers calculate absolute attitude in three dimensions from celestial measurements. Sigel and Wettergreen [17] developed simulations that used a star tracker to calculate rover position for a lunar rover, but not full heading. Xiaolin and Jiancheng [18] developed algorithms for calculating rover position from star elevation measurements and tested them in hardware-in-the-loop simulations.

In this paper, we present a star-tracker-based attitude correction algorithm for use with full-dark odometry. This paper provides the concept, theory, and the results from outdoor experiments using a real rover (Figure 1), inclinometer, and star tracker (Figure 2). To the best of the authors' knowledge, this represents the first time a star tracker has been deployed on a real rover. The data consists of 7 hours of rover operations and just under 2.5 kilometres of driving (Figure 3), with a range of elevations (Figure 4). The estimates from wheel odometry and VO are compared with and without the star tracker measurements. This algorithm is suitable for odometry generated from wheel encoders, active stereo VO, lidar-based VO, or other sources of odometry that do not require the presence of ambient light.

This paper is structured as follows. Section 2 presents the algorithms used to calculate absolute heading, as first
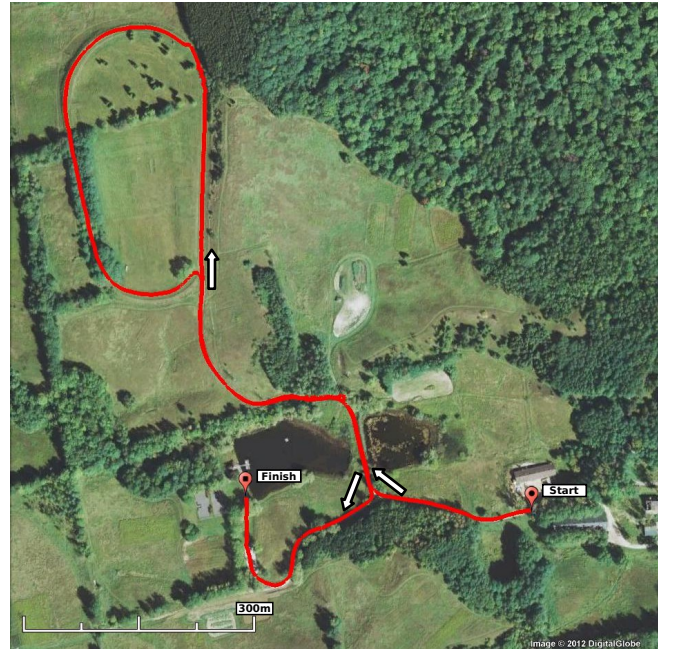

Figure 3. The path taken by the rover as calculated by post-processed DGPS.

presented by Enright et al. [19], and calculates the optimal estimate of the global rover positions. Section 3 presents the methods used to collect the experimental data while Section 4 presents the results of the proposed algorithms on the collected data. Section 5 discusses the challenges encountered and the ongoing work to address them.

2. ALGORITHM

This section is divided into two parts. In the first section we present the algorithm to calculate rover attitude from star tracker measurements and in the second we provide the batch optimization formulation to combine relative odometry measurements with absolute orientation measurements. For generality, we assume that the odometry measurements are 6 Degree-of-Freedom (DOF) transformation matrices, and the orientation measurements are 3 DOF rotation matrices. The estimate is a batch optimization completed at the end of the traverse, but it could also be carried out in an online filtering mode. The batch approach allows infrequent attitude measurements to correct the entire traverse and it also enables loop closure to be incorporated into future work which plans to use a place-recognition algorithm [20].

Star Tracker Attitude Measurements

As described by Enright et al. [19], star tracker measurements can be post-processed to remove the effect of atmospheric refraction using the gravity vector calculated from the inclinometer. After correction, the star vectors are rematched to the star catalogue generating revised attitude estimates (Figure 5). These raw measurements are estimates of the star tracker orientation in the Earth-Centred Inertial (ECI) frame at time k, $\mathbf{C}_{S_k I}$, and, in order to provide meaningful attitude data, must be transformed to measurements relative to the Earth-Centred Earth-Fixed (ECEF) frame (Table 1),

$$\mathbf{C}_{S_k F} := \mathbf{C}_{S_k I} \mathbf{C}_{IF},$$

Table 1. Frame Definitions

Frame	Designation	X	Y	Z
Earth Centred Inertial (J2000)	I	Vernal Equinox	–	North Pole
Earth Centred, Earth Fixed	F	Prime Meridian	–	North Pole
Star Tracker	S	Data Connector	–	Lens Boresight
Vehicle	V	Rover Heading	–	Parallel to Star Tracker z-axis
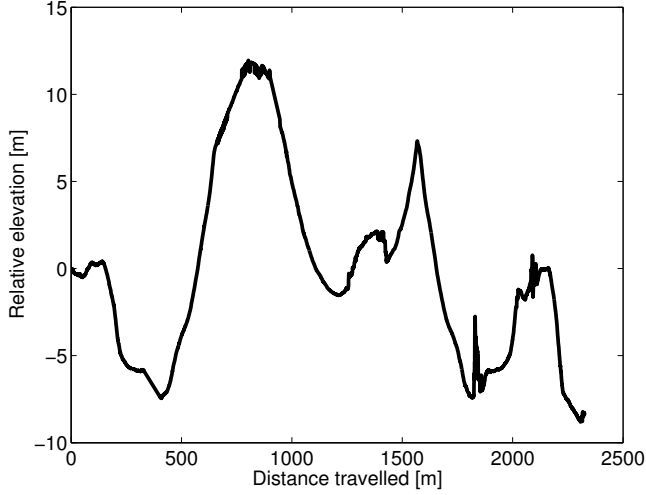
Figure 4. Elevation versus distance travelled.

Figure 5. A sample measurement showing the star tracker detecting stars ($\times$) and matching them to a catalogue of known stars ($\circ$).

so that the effects of the Earth's rotation are removed. The transformation from ECI to ECEF, $\mathbf{C}_{IF}$, is computed via the Greenwich Apparent Sidereal Time, from any available and reliable clock reference. The initial orientation of the sensor, $\mathbf{C}_{S_0 F}$, is averaged before the start of the rover traverse to reduce error. During the traverse, the relative orientation of the k-th measurement, $\mathbf{C}_{S_k S_0}$, is then

$$\mathbf{C}_{S_k S_0} = \mathbf{C}_{S_k I} \mathbf{C}_{IF} \mathbf{C}_{F S_0}. \qquad (1)$$

We can estimate the covariance of the relative attitude by considering a first-order model of error propagation. We perturb the measurements in (1) in terms of error rotations, ϕ, ignoring any contributions from the initial orientation, $\mathbf{C}_{F S_0}$, to obtain

$$\left(\mathbf{1} - \phi_{S_k S_0}^{\times}\right) \mathbf{C}_{S_k S_0} = \left(\mathbf{1} - \phi_{S_k I}^{\times}\right) \mathbf{C}_{S_k I} \qquad (2)$$
$$\times \left(\mathbf{1} - \phi_{IF}^{\times}\right) \mathbf{C}_{IF} \mathbf{C}_{F S_0},$$

where $\mathbf{1}$ is the identity matrix and the operator, $(\cdot)^{\times}$, is defined for a 3×1 vector, $\mathbf{u}$, as

$$\mathbf{u}^{\times} = \begin{bmatrix} u_1 \\ u_2 \\ u_3 \end{bmatrix}^{\times} := \begin{bmatrix} 0 & -u_3 & u_2 \\ u_3 & 0 & -u_1 \\ -u_2 & u_1 & 0 \end{bmatrix}.$$

Expanding and discarding second-order terms, (2) simplifies to

$$\phi_{S_k S_0} \approx \phi_{S_k I} + \mathbf{C}_{S_k I} \phi_{IF}, \qquad (3)$$

where the error vector, ϕ_{IF}, captures the uncertainty in time. As this is a pure z-axis rotation, we can note that this error will be a function of the Earth sidereal rate, ω_e, and the
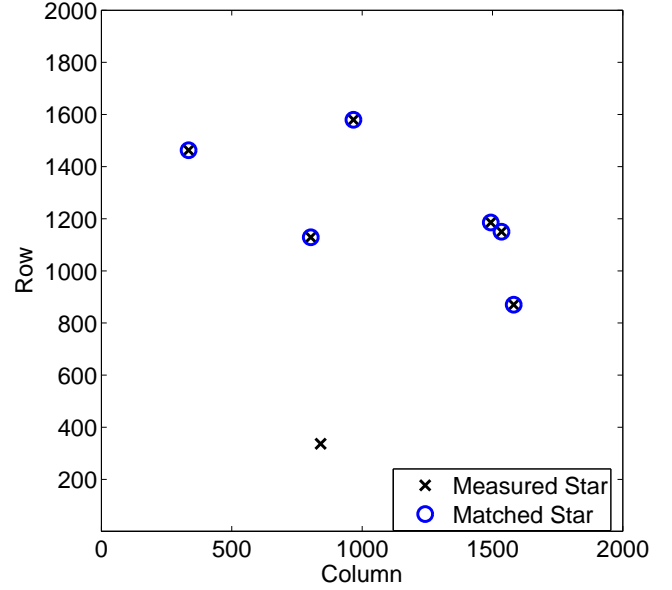
uncertainty in time, δ_t, which is of the form

$$\phi_{IF} = \begin{bmatrix} 0 \\ 0 \\ \omega_e \delta_t \end{bmatrix}. \qquad (4)$$

The covariance of the measurement, $\mathbf{P}_{S_k S_0}$, is defined as

$$\mathbf{P}_{S_k S_0} := E\left[\phi_{S_k S_0} \phi_{S_k S_0}^T\right].$$

Assuming uncorrelated errors and substituting (3), this simplifies to

$$\mathbf{P}_{S_k S_0} = \mathbf{P}_{S_k I} + \mathbf{C}_{S_k I} \mathbf{P}_{IF} \mathbf{C}_{IS_k},$$

where

$$\mathbf{P}_{S_k I} := E\left[\phi_{S_k I} \phi_{S_k I}^T\right],$$
$$\mathbf{P}_{IF} := E\left[\phi_{IF} \phi_{IF}^T\right],$$

are the covariance contributions of the inertial-attitude and Earth-rotation, respectively. Using Schuster's information matrix formulation [21], we can calculate the inertial-attitude covariance, $\mathbf{P}_{S_k I}$, from the inertial-frame star vectors, $\mathbf{m}$, as

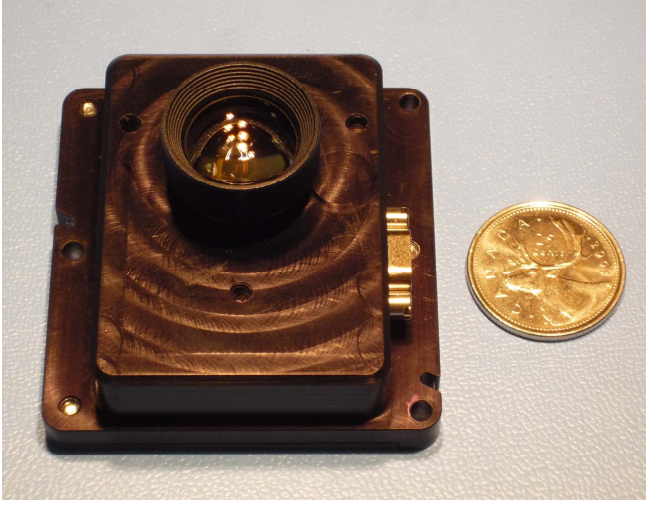$$\mathbf{P}_{S_k I}^{-1} = \sum_i \frac{1}{\sigma_i^2} \left(\mathbf{1} - \mathbf{m}_i \mathbf{m}_i^T\right),$$

Figure 6. The S3S ST16 star tracker.

Figure 7. Locations of odometry measurements (green), star tracker measurements (black) and subsampled star tracker measurements (red).

where σ_i^2 is the angular variance associated with the i-th star vector, $\mathbf{m}_i$. From (4), the Earth-rotation contribution to the covariance, $\mathbf{P}_{IF}$, expressed in the I-frame, must have the form

$$\mathbf{P}_{IF} = \begin{bmatrix} 0 & 0 & 0 \\ 0 & 0 & 0 \\ 0 & 0 & \omega_e^2 \sigma_t^2 \end{bmatrix},$$

where σ_t^2 is the variance associated with the time measurement. Table 2 shows the numerical values used for these parameters for this paper.

Rover Pose Estimation

We wish to obtain an accurate estimate of the global positions of the rover throughout its traverse. Given a series of relative odometric measurements as 6 DOF transformation matrices, $\mathbf{T}_{V_k V_{k-1}}$, with associated covariances, $\mathbf{U}_{V_k V_{k-1}}$, as well as periodic, absolute orientation measurements as 3 DOF rotation matrices, $\tilde{\mathbf{C}}_{S_k S_0}$, with associated covariances, $\mathbf{P}_{S_k S_0}$, we can achieve this by finding the optimal estimate of the global transformations from the first pose, $\mathbf{T}_{V_k V_0}^*$, that minimizes a cost function,

$$J := \frac{1}{2} \sum_k \left(\delta\boldsymbol{\epsilon}_{V_k V_{k-1}}^T \mathbf{U}_{V_k V_{k-1}}^{-1} \delta\boldsymbol{\epsilon}_{V_k V_{k-1}} \right. \tag{5}$$
$$\left. + \; \delta\boldsymbol{\psi}_{S_k S_0}^T \mathbf{P}_{S_k S_0}^{-1} \delta\boldsymbol{\psi}_{S_k S_0} \right).$$

Our errors at the current iteration, $\delta\boldsymbol{\epsilon}_{V_k V_{k-1}}$ and $\delta\boldsymbol{\psi}_{S_k S_0}$, are defined as

$$e^{-\delta\boldsymbol{\epsilon}_{V_k V_{k-1}}^{\boxplus}} := \tilde{\mathbf{T}}_{V_k V_{k-1}} \mathbf{T}_{V_{k-1} V_0} \mathbf{T}_{V_k V_0}^{-1}, \tag{6}$$
$$e^{-\delta\boldsymbol{\psi}_{S_k S_0}^{\times}} := \tilde{\mathbf{C}}_{S_k S_0} \mathbf{C}_{VS}^T \mathbf{C}_{V_k V_0}^T \mathbf{C}_{VS}. \tag{7}$$

with the operator, $(\cdot)^{\boxplus}$, defined for a 6×1 vector, $\mathbf{w}$, as

$$\mathbf{w}^{\boxplus} = \begin{bmatrix} \mathbf{u} \\ \mathbf{v} \end{bmatrix}^{\boxplus} := \begin{bmatrix} \mathbf{v}^{\times} & -\mathbf{u} \\ \mathbf{0}^T & 0 \end{bmatrix}.$$

Our pose estimates, $\mathbf{T}_{V_k V_0}$, are transformation matrices consisting of the rotation from V_0 to V_k, $\mathbf{C}_{V_k V_0}$, and translation
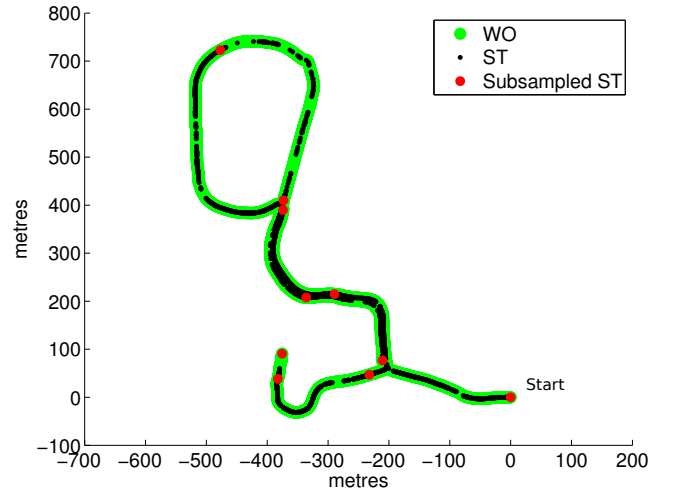
Table 2. Numerical quantities for absolute orientation calculations.

Quantity	Value
σ_t	$1\,\text{s}$
ω_e	$7.2925 \times 10^{-5}\,\text{rad/s}$
σ_i	$5.36 \times 10^{-5}\,\text{rad}$

from V_0 to V_K expressed in frame V_0, $\mathbf{r}_{V_0}^{V_k V_0}$,

$$\mathbf{T}_{V_k V_0} =: \begin{bmatrix} \mathbf{C}_{V_k V_0} & -\mathbf{C}_{V_k V_0} \mathbf{r}_{V_0}^{V_k V_0} \\ \mathbf{0}^T & 1 \end{bmatrix}.$$

Assuming that the differences between estimates at subsequent iterations are small, we can express the new estimate in terms of perturbations, $\delta\boldsymbol{\pi}_{V_k V_0}$ and $\delta\boldsymbol{\phi}_{V_k V_0}$, on the previous estimates, $\overline{\mathbf{T}}_{V_k V_0}$ and $\overline{\mathbf{C}}_{V_k V_0}$,

$$\mathbf{T}_{V_k V_0} := e^{-\delta\boldsymbol{\pi}_{V_k V_0}^{\boxplus}} \overline{\mathbf{T}}_{V_k V_0}, \tag{8}$$
$$\mathbf{C}_{V_k V_0} := e^{-\delta\boldsymbol{\phi}_{V_k V_0}^{\times}} \overline{\mathbf{C}}_{V_k V_0}, \tag{9}$$

and define the errors at the previous iteration, $\delta\overline{\boldsymbol{\epsilon}}_{V_k V_{k-1}}$ and $\delta\overline{\boldsymbol{\psi}}_{S_k S_0}$, analogously to (6) and (7) as

$$e^{-\delta\overline{\boldsymbol{\epsilon}}_{V_k V_{k-1}}^{\boxplus}} := \tilde{\mathbf{T}}_{V_k V_{k-1}} \overline{\mathbf{T}}_{V_{k-1} V_0} \overline{\mathbf{T}}_{V_k V_0}^{-1}, \tag{10}$$
$$e^{-\delta\overline{\boldsymbol{\psi}}_{S_k S_0}^{\times}} := \tilde{\mathbf{C}}_{S_k S_0} \mathbf{C}_{VS}^T \overline{\mathbf{C}}_{V_k V_0}^T \mathbf{C}_{VS}. \tag{11}$$

Substituting (8) and (9) into (6) and (7) yields

$$e^{-\delta\boldsymbol{\epsilon}_{V_k V_{k-1}}^{\boxplus}} := \tilde{\mathbf{T}}_{V_k V_{k-1}} e^{-\delta\boldsymbol{\pi}_{V_{k-1} V_0}^{\boxplus}} \overline{\mathbf{T}}_{V_{k-1} V_0} \overline{\mathbf{T}}_{V_k V_0}^{-1} e^{\delta\boldsymbol{\pi}_{V_k V_0}^{\boxplus}},$$
$$e^{-\delta\boldsymbol{\psi}_{S_k S_0}^{\times}} := \tilde{\mathbf{C}}_{S_k S_0} \mathbf{C}_{VS}^T \overline{\mathbf{C}}_{V_k V_0}^T e^{\delta\boldsymbol{\phi}_{V_k V_0}^{\times}} \mathbf{C}_{VS}.$$
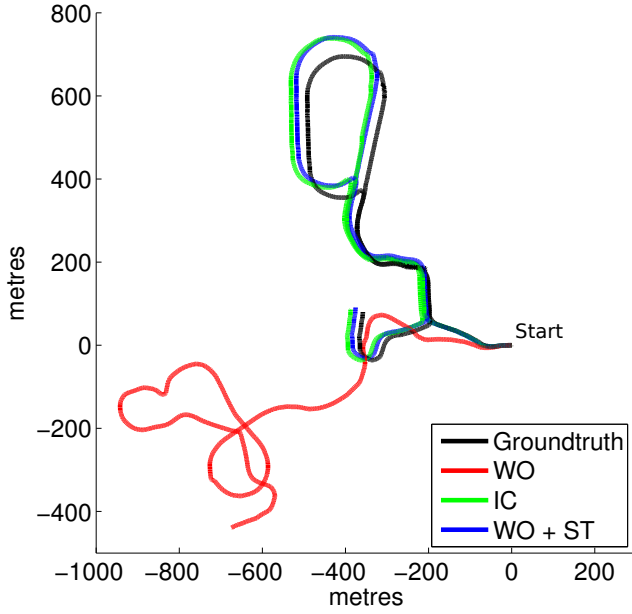
4

Figure 8. Estimates produced from wheel odometry corrected with all star tracker attitude measurements (blue) plotted with the initial condition (green), the DGPS groundtruth (black), and the wheel odometry (red)

Rearranging and applying (10) and (11), respectively, we are left with

$$e^{-\delta\boldsymbol{\epsilon}_{V_k V_{k-1}}^{\boxplus}} \approx e^{-\delta\overline{\boldsymbol{\epsilon}}_{V_k V_{k-1}}^{\boxplus}}$$
$$\times \; e^{\left(-\overline{\mathbf{T}}_{V_k V_0}^{\boxdot} \delta\boldsymbol{\pi}_{V_{k-1} V_0}\right)^{\boxplus}} e^{\delta\boldsymbol{\pi}_{V_k V_0}^{\boxplus}},$$
$$e^{-\delta\boldsymbol{\psi}_{S_k S_0}^{\times}} \approx e^{-\delta\overline{\boldsymbol{\psi}}_{S_k S_0}^{\times}} e^{\left(\mathbf{C}_{VS}^{T} \delta\boldsymbol{\phi}_{V_k V_0}\right)^{\times}}.$$

This can be rewritten finally as

$$\delta\boldsymbol{\epsilon}_{V_k V_{k-1}} \approx \delta\overline{\boldsymbol{\epsilon}}_{V_k V_{k-1}} - \mathbf{H}_{k,k-1}\mathbf{B}_{k,k-1}\delta\mathbf{x},$$
$$\delta\boldsymbol{\psi}_{S_k S_0} \approx \delta\overline{\boldsymbol{\psi}}_{S_k S_0} - \mathbf{G}_{k,0}\mathbf{B}_{k,0}\delta\mathbf{x},$$

where

$$\mathbf{H}_{k,k-1} := \begin{bmatrix} \mathbf{1} & -\overline{\mathbf{T}}_{V_k V_0}^{\boxdot} \end{bmatrix},$$
$$\mathbf{G}_{k,0} := \begin{bmatrix} \mathbf{0} & \mathbf{C}_{VS}^{T} & \mathbf{0} & \mathbf{0} \end{bmatrix},$$
$$\delta\mathbf{x}_{k,k-1} =: \mathbf{B}_{k,k-1}\delta\mathbf{x},$$
$$\delta\mathbf{x}_{k,k-1} := \begin{bmatrix} \delta\boldsymbol{\pi}_{V_k V_0} \\ \delta\boldsymbol{\pi}_{V_{k-1} V_0} \end{bmatrix},$$
$$\delta\boldsymbol{\pi}_{V_k V_0} := \begin{bmatrix} \delta\boldsymbol{\rho}_{V_k V_0} \\ \delta\boldsymbol{\phi}_{V_k V_0} \end{bmatrix},$$

and the operator, $(\cdot)^{\boxdot}$, is defined for any transformation matrix, $\mathbf{T}$, as

$$\mathbf{T}^{\boxdot} = \begin{bmatrix} \mathbf{C} & -\mathbf{Cr} \\ \mathbf{0}^{T} & 1 \end{bmatrix}^{\boxdot} := \begin{bmatrix} \mathbf{C} & \mathbf{Cr}^{\times} \\ \mathbf{0} & \mathbf{C} \end{bmatrix}.$$

The minimum of (5) may be found be setting

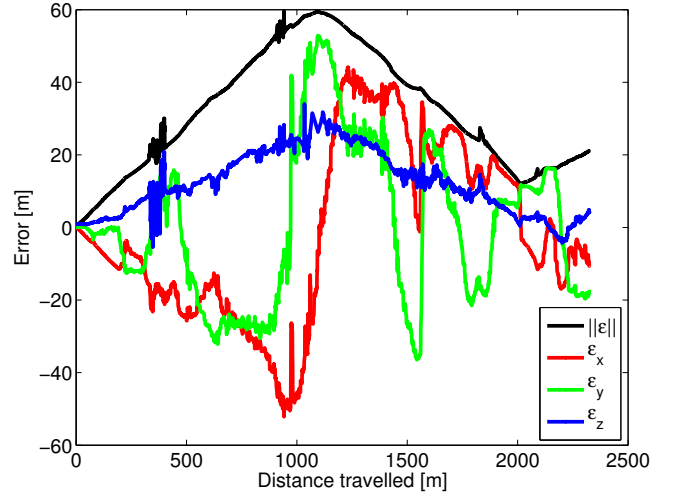$$\frac{\partial J}{\partial \delta\mathbf{x}}^{T} = \mathbf{0},$$

Figure 9. The estimate error plotted versus distance travelled for the entire 2845 star tracker data set. The increase in error variability in the ranges 350 m – 410 m and 925 m – 975 m is the result of error in the groundtruth GPS estimate.

Table 3. Error for the frequent star-tracker-measurement solution, $\boldsymbol{\epsilon}$, in meters expressed in the local rover frames

	Mean	St. Dev.	Min.	Max.	Final
$\|\boldsymbol{\epsilon}\|$	31.9	16.5	0.9	59.7	21.0
ϵ_x	-1.5	24.1	-52.2	44.2	-10.5
ϵ_y	0.5	21.9	-36.5	52.9	-17.7
ϵ_z	12.4	8.8	-5.4	34.0	4.2

whereupon we arrive at a system of equations,

$$\boldsymbol{\mathcal{V}}\,\delta\mathbf{x} = -\mathbf{v}, \qquad (12)$$

where

$$\boldsymbol{\mathcal{V}} := \sum_k \Big(\mathbf{B}_{k,k-1}^{T} \mathbf{H}_{k,k-1}^{T} \mathbf{U}_{V_k V_{k-1}}^{-1} \mathbf{H}_{k,k-1} \mathbf{B}_{k,k-1}$$
$$+ \; \mathbf{B}_{k,0}^{T} \mathbf{G}_{k,0} \mathbf{P}_{S_k S_0}^{-1} \mathbf{G}_{k,0} \mathbf{B}_{k,0} \Big),$$
$$\mathbf{v} := -\sum_k \Big(\mathbf{B}_{k,k-1}^{T} \mathbf{H}_{k,k-1}^{T} \mathbf{U}_{V_k V_{k-1}}^{-1} \delta\overline{\boldsymbol{\epsilon}}_{V_k V_{k-1}}$$
$$+ \; \mathbf{B}_{k,0}^{T} \mathbf{G}_{k,0} \mathbf{P}_{S_k S_0}^{-1} \delta\overline{\boldsymbol{\psi}}_{S_k S_0} \Big).$$

Assuming an initial estimate from the odometry, we can solve (12) for $\delta\mathbf{x}$ and get updated estimates from

$$\mathbf{T}_{V_k V_0} \leftarrow e^{-\delta\boldsymbol{\pi}_{V_k V_0}^{\boxplus}} \overline{\mathbf{T}}_{V_k V_0}.$$

We iterate these steps until the estimate update is tolerably small to obtain a pose graph of absolute transformations from the first pose, $\mathbf{T}_{V_k V_0}^{*}$. This representation allows for future problems to include loop closures and for measurements to affect estimates at all both future and past timesteps.

3. EXPERIMENT

The algorithm was tested on experimental data collected with a real rover and star tracker (Figure 2). A Clearpath
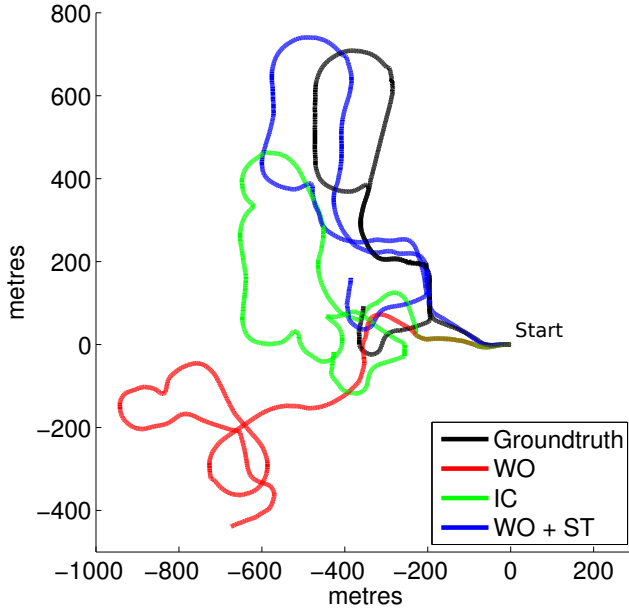
Figure 10. Estimates produced from wheel odometry corrected with only 10 star tracker attitude measurements (blue) plotted with the initial condition (green), the DGPS groundtruth (black), and the wheel odometry (red).

Husky A200 (Figure 1) was equipped with a DGPS, and a Sinclair Interplanetary S3S ST-16 star tracker (Figure 6) and driven just under 2.5 kilometres through the Koffler Scientific Reserve at Jokers Hill (KSR) (Figure 3) on the night of September 16th, 2012, a day after a new moon, in clear conditions.

The A200 is a 4-wheel differential-drive rover with two motors, each equipped with quadrature encoders with a resolution of approximately 20000 pulse/metre. While the rover is electric, it was equipped for long-term autonomy with a kilowatt gasoline generator. In order to calculate the actual rover position during the traverse, the rover was equipped with a differential GPS receiver and an RTK base station was deployed at a central location.

The rover was driven manually via remote control for the duration of the experiment. Wheel odometry was logged at 10 Hz and star tracker attitude at 1 Hz. It was expected that the rover motion would frequently interfere with star tracker measurements, as the images are blurred when rotational motion exceeds 2–3 °/s. In practice, however, it was found that rates this fast were rare, and the star tracker was capable of measuring attitude continuously during rover motion (Figure 7). As a result, the rover was driven continuously for the 7 hours that it took to travel the almost 2.5 kilometres. The route had significant elevation change, dropping more than 8 meters below the starting position and rising almost 12 meters above it (Figure 4).

Star Tracker

The Sinclair Interplanetary S3S ST-16 (Figure 6) is an autonomous star tracker designed for nanosatellite applications featuring low mass (90 g), low power (< 1 W), small volume (59 mm $\times$56 mm $\times$32.5 mm), and a relatively large Field of View (FOV) ($15°\times21°$). These features also make it an attractive option for mobile rovers and long-term autonomy.
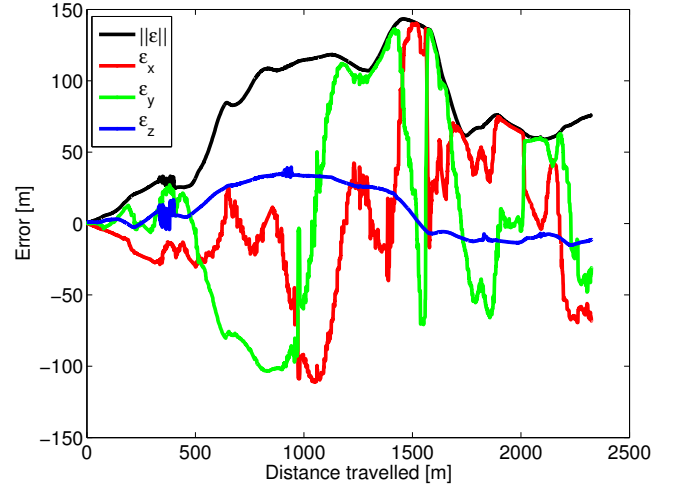

Figure 11. The estimate error plotted versus distance travelled for the 10 star tracker data set. The increase in error variability in the ranges 350 m – 410 m and 925 m – 975 m is the result of error in the groundtruth GPS estimate.

Table 4. Error for the subsampled star-tracker-measurement solution, ϵ, in metres expressed in the local rover frames

	Mean	St. Dev.	Min.	Max.	Final
$\|\|\epsilon\|\|$	77.3	39.6	0.9	143.4	75.8
ϵ_x	1.5	51.4	-111.0	140.3	-68.0
ϵ_y	7.5	66.9	-103.4	136.2	-31.4
ϵ_z	9.0	17.3	-15.2	39.5	-11.4

The large FOV gives the S3S the ability to detect an increased number of stars compared to other star trackers, allowing for a design that relies on the detection of bright stars (magnitude 5.75 or brighter) over a wide area of the sky instead of dimmer stars distributed in a smaller area. This design is advantageous for atmospheric operations, as viewing conditions (e.g., light pollution, clouds, etc.) place a lower bound on the visibility of dim stars. Thus, the S3S should be more reliable in these applications than other sensors that require the detection of dimmer stars. The sensor telemetry includes attitude relative to the J2000 Earth-Centred Inertial frame (Table 1), attitude covariance, and extended information about the stars in view. While not used in these experiments, the firmware can also correct for atmospheric refraction online eliminating the need for post-processing. For the purpose of these experiments, the Greenwich Apparent Sidereal Time was calculated in post-processing from the GPS clock.

4. RESULTS

In this section we discuss the results of two simulated experiments generated from the one data set: (i) a experiment containing 2845 star tracker measurements, and (ii) a experiment containing only 10 star tracker measurements.

Frequent Star Tracker Measurements

The wheel odometry was post-processed into 5-second increments and assigned the nearest star tracker measurement that occurred within 1 second. This resulted in a traverse of 5123 poses with 2845 star tracker measurements that were
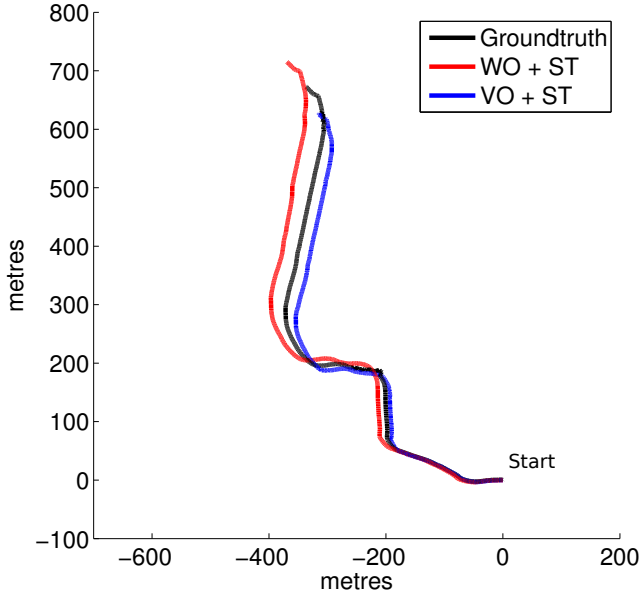
Figure 12. Estimates produced from star-tracker-corrected lidar VO (blue) and wheel odometry (red) plotted with the DGPS groundtruth (black).

Figure 13. The 3D estimate error for visual- (blue) and wheel- (red) odometry estimates corrected by the full star tracker measurements versus distance travelled over the first 1 km of the traverse. The increase in error variability between 350 m – 410 m and 925 m – 975 m is the result of error in the groundtruth GPS estimate.

used to verify the algorithm described in Section 2. The batch optimization initial conditions consisted of a poor-man's sensor fusion that replaced the odometric rotation estimate with the star tracker measurement whenever available (Figure 8).

The results of the optimization, $\mathbf{x}_{\text{est}}$, were compared to post-processed differential GPS measurements, $\mathbf{x}_{\text{gps}}$, of the rover's actual location during the traverse. The first 100 poses, approximately 100 m, were used to calculate the rotation from GPS frame to vehicle frame.

The resulting position error,

$$\boldsymbol{\epsilon} := \mathbf{x}_{\text{gps}} - \mathbf{x}_{\text{est}}, \tag{13}$$

was found to be significantly better than simple wheel odometry (Figure 8). The error of the final position was found to be 21 m, or 0.85% of the distance travelled. (Figure 9, Table 3).

The optimization was performed in Matlab on an Intel Core i7 2.67 GHz processor running 64bit Ubuntu Linux with 4 GB of memory. The presented wheel odometry results took approximately 2.75 hours of processing time.

Subsampled Star Tracker Measurements

To emulate applications where rover speed does not permit continuous operation of the star tracker, the attitude measurements were subsampled to approximately a spacing of every 250 metres (Figure 7). The resulting 10 measurements were used as attitude corrections on the 5123 rover poses in a second optimization problem and the results of the optimization are presented. Poor-man's sensor fusion was again used as the initial conditions. As in the previous section, the first 100 poses of the solution, approximately 100 m, were used to calculate the rotation from GPS frame to vehicle frame and the results were compared to the differential GPS.

The resulting position error was found to be significantly better than simple wheel odometry and the poor-man's sensor
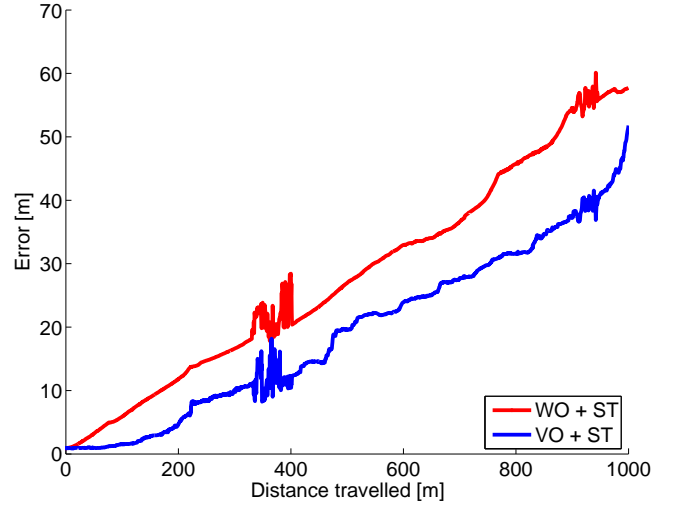
fusion (Figure 10). The error of the final position was found to be 75.8 m, or 3.0% of the distance travelled. (Figure 11, Table 4).

The optimization was performed in Matlab on an Intel Core i7 2.67 GHz processor running 64bit Ubuntu Linux with 4 GB of memory. The presented wheel odometry results took 45 minutes of processing.

5. DISCUSSION & FUTURE WORK

The results of Section 4 demonstrate that, when the rover is driving slow enough to collect frequent star tracker measurements (Figure 7), the batch optimization presented in Section 2 provides a better estimate than the wheel odometry; however, it is not sufficiently more accurate than the poor-man's sensor fusion that replaces the odometric rotation estimate with the star tracker measurement whenever available. In this case, an Extended Kalman Filter (EKF) may provide a sufficient improvement to the of poor-man's sensor fusion without the cost of a batch estimate.

If, however, the rover operates at speeds too high to collect star tracker measurements, or the star tracker measurements are otherwise very infrequent, the presented batch algorithm clearly provides a better estimate than wheel odometry alone or the poor-man's sensor fusion. The batch formulation allows for measurements to affect estimates at all timesteps, resulting in a smoother and more accurate solution, and allowing for the future inclusion of place recognition and loop closure.

The timing results in this paper are from an unoptimized Matlab implementation. It is expected that the computational performance could be significantly improved by efficient implementations or advanced techniques, such as Incremental Smoothing and Mapping (iSAM) [22]. As is, however, the estimator still ran in less time than the rover took to drive the 2.5 kilometre traverse.
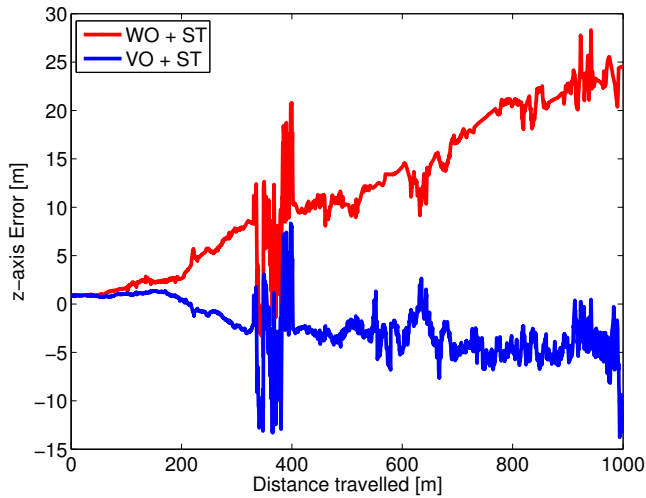
Figure 14. The z component of estimate error for visual- (blue) and wheel- (red) odometry estimates corrected by the full star tracker measurements versus distance travelled over the first 1 km of the traverse. The increase in error variability between 350 m – 410 m and 925 m – 975 m is the result of error in the groundtruth GPS estimate.

(a) Intensity (b) SURF Features (c) Frame-to-frame feature motion

Figure 15. The intensity-image VO pipeline. An intensity image (a) is acquired from the SICK lidar and processed for SURF features (b). Features are matched between frames (c) to provide a motion estimate.

The combination of wheel odometry, the star tracker, and the batch optimization make the presented results quite attractive in terms of accuracy and simplicity. The presented results rival VO with simpler sensors; however, there remain areas for improvement. Wheel odometry alone can only estimate rover motion on a 2D plane, and wheel slip makes it inaccurate over long distances. For these reasons, lighting-invariant VO is worth investigating for further improvements. While there has been some success in using light sources in conjunction with stereo cameras and traditional VO [13], [14], they would require design and operational procedures to mitigate light pollution for the star tracker. Regardless of the VO solution, optical contamination created by the rover, e.g., dust, would remain an important, but ultimately tractable, deployment problem.

Success by McManus et al. [15] and Dong and Barfoot [16] using lidar intensity images for VO suggest that a lidar is a natural choice for improved odometric measurements for this mission scenario. In order to investigate this potential, the Husky A200 was also equipped with a SICK scanning lidar during the experiment (Figure 15). The SICK was mounted in a vertical-scan configuration on a pan-tilt unit that oscillated it left-to-right. Intensity-based VO using the resulting data provided better odometric estimates than wheel odometry for portions of the traverse (Figure 13). After approximately 1 kilometre, the lidar-VO-based estimate with star tracker measurements has less error than the equivalent wheel-odometry-based estimate (51.0 m to 57.7 m, Figure 12). As VO provides full 6 DOF estimates, the z-component of the resulting error is significantly lower (Figure 14). After this first kilometre, we experienced a large grass section around the northern-most turn of the traverse and were unable to track features for an extended period of time, leading to poor estimator performance. As with stereo-camera VO, tracking features in grass remains a formidable challenge and more work is required to address the issues arising from vegetation. In general, performing VO on data collected from a sensor with such high levels of motion distortion is an ongoing research topic [23].
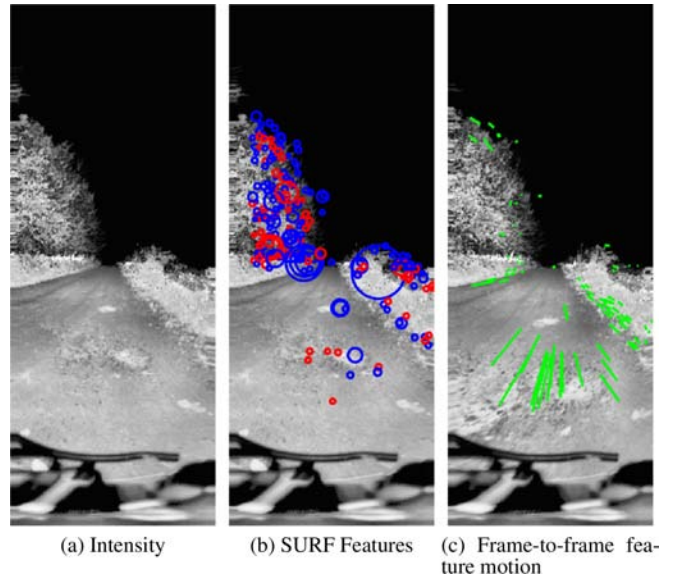
6. CONCLUSIONS

This paper presented a method to correct odometric estimates for drift and/or bias using a star tracker during full-dark rover operations. The algorithm was tested on a real rover with a star tracker and inclinometer, which, to the best of the authors' knowledge, is a robotic first. The results presented show that the algorithm is extremely successful at creating an accurate estimate despite using simple, low-computational-cost sensors, such as wheel odometry, over extended distances. When using the entire set of attitude measurements the final position error was 21 metres over a traverse of just under 2.5 kilometres, or 0.85% of the total distance travelled. When the attitude measurements were limited to approximately every 250 metres, only 10 for the entire traverse, the resulting final position error was 75.8 metres, or 3.0% of the total distance travelled.

The results also highlight the challenges of using lidar-based VO instead of wheel odometry. When there were sufficient features, the lidar-based VO outperformed the wheel odometry; however, significant periods without adequate features made the complete estimate inaccurate. This is a challenge that was further amplified by the scanning nature of the SICK lidar and the vegetation-heavy test environment at KSR; however, based on these results, we believe that star trackers will provide suitable attitude correction for lidar VO.

APPENDICES
A. MATRIX OPERATOR DEFINITIONS

Given

$$\mathbf{w} := \begin{bmatrix} \mathbf{u} \\ \mathbf{v} \end{bmatrix}, \qquad \mathbf{u} := \begin{bmatrix} u_1 \\ u_2 \\ u_3 \end{bmatrix}, \qquad \mathbf{v} := \begin{bmatrix} v_1 \\ v_2 \\ v_3 \end{bmatrix},$$

and

$$\mathbf{T} = \begin{bmatrix} \mathbf{C} & -\mathbf{Cr} \\ \mathbf{0}^T & 1 \end{bmatrix},$$

the following operators are defined:

$$\mathbf{u}^{\times} := \begin{bmatrix} 0 & -u_3 & u_2 \\ u_3 & 0 & -u_1 \\ -u_2 & u_1 & 0 \end{bmatrix}, \quad \mathbf{w}^{\boxplus} := \begin{bmatrix} \mathbf{v}^{\times} & -\mathbf{u} \\ \mathbf{0}^T & 0 \end{bmatrix},$$

$$\mathbf{T}^{\boxdot} := \begin{bmatrix} \mathbf{C} & \mathbf{Cr}^{\times} \\ \mathbf{0} & \mathbf{C} \end{bmatrix}.$$

B. MATRIX OPERATOR IDENTITIES

Given the definitions in Appendix A, we have the following identities:

$$(\alpha\mathbf{u} + \beta\mathbf{v})^{\times} \equiv \alpha\mathbf{u}^{\times} + \beta\mathbf{v}^{\times},$$

$$\mathbf{u}^{\times^T} \equiv -\mathbf{u}^{\times}, \quad \mathbf{u}^{\times}\mathbf{u} \equiv \mathbf{0}, \quad \mathbf{u}^{\times}\mathbf{v} \equiv -\mathbf{v}^{\times}\mathbf{u},$$

$$(\mathbf{T}_1\mathbf{T}_2)^{\boxdot} \equiv \mathbf{T}_1^{\boxdot}\mathbf{T}_2^{\boxdot}, \quad \mathbf{T}^{\boxdot^{-1}} \equiv \mathbf{T}^{-1\boxdot},$$

$$e^{(\mathbf{T}^{\boxdot}\mathbf{w})^{\boxplus}} \equiv \mathbf{T}e^{\mathbf{w}^{\boxplus}}\mathbf{T}^{-1},$$

$$(\mathbf{Cu})^{\times} \equiv \mathbf{Cu}^{\times}\mathbf{C}^T,$$

$$e^{(\mathbf{Cu})^{\times}} \equiv \mathbf{C}e^{\mathbf{u}^{\times}}\mathbf{C}^T,$$

where α and β are scalars, $\mathbf{T}$ is a transformation matrix, $\mathbf{C}$ is a rotation matrix, and $\mathbf{u}$, $\mathbf{v}$, and $\mathbf{w}$ are vectors as defined in Appendix A.

ACKNOWLEDGMENTS

REFERENCES

[1] R. Volpe, "Mars rover navigation results using sun sensor heading determination," in *Proc. of the IEEE/RSJ Int. Conf. on Intelligent Robots and Systems (IROS)*, vol. 1, 1999, pp. 460–467.

[2] J. Bakambu, V. Polotski, and P. Cohen, "Heading-aided odometry and range-data integration for positioning of autonomous mining vehicles," in *Proc. of the IEEE Int. Conf. on Control Applications*, 2000, pp. 279–284.

[3] E. T. Baumgartner, H. Aghazarian, A. Trebi-Ollennu, T. L. Huntsberger, and M. S. Garrett, "State estimation and vehicle localization for the fido rover," *Proc. of SPIE Sensor Fusion and Decentralized Control in Robotic Systems III*, vol. 4196, pp. 329–336, 2000.

[4] J. B. Balaram, "Kinematic state estimation for a mars rover," *Robotica*, vol. 18, no. 03, pp. 251–262, 2000.

[5] P. Lamon and R. Siegwart, "Inertial and 3d-odometry fusion in rough terrain - towards real 3d navigation," in *Proc. of the IEEE/RSJ Int. Conf. on Intelligent Robots and Systems (IROS)*, vol. 2, 28 Sep. - 2 Oct. 2004, pp. 1716–1721.

[6] L. Matthies and S. Shafer, "Error modeling in stereo navigation," *IEEE Journal of Robotics and Automation*, vol. 3, no. 3, pp. 239 –248, Jun. 1987.

[7] K. Ali, C. Vanelli, J. Biesiadecki, M. Maimone, Y. Cheng, A. San Martin, and J. Alexander, "Attitude and position estimation on the mars exploration rovers," in *Proc. of the IEEE Int. Conf. on Systems, Man and Cybernetics*, vol. 1, Oct. 2005, pp. 20–27.

[8] C. F. Olson, L. H. Matthies, M. Schoppers, and M. W. Maimone, "Rover navigation using stereo ego-motion," *Robotics and Autonomous Systems*, vol. 43, no. 4, pp. 215 – 229, 2003.

[9] J. Enright, P. Furgale, and T. Barfoot, "Sun sensing for planetary rover navigation," in *Proc. of the IEEE Aerospace Conf.*, Mar. 2009, pp. 1–12.

[10] P. Furgale, J. Enright, and T. Barfoot, "Sun sensor navigation for planetary rovers: Theory and field testing," *IEEE Transactions on Aerospace and Electronic Systems*, vol. 47, no. 3, pp. 1631 –1647, Jul. 2011.

[11] A. Lambert, P. T. Furgale, T. D. Barfoot, and J. Enright, "Field testing of visual odometry aided by a sun sensor and inclinometer," *Journal of Field Robotics,* special issue on "Space Robotics", vol. 29, no. 3, pp. 426–444, May - Jun. 2012.

[12] A. Colaprete, P. Schultz, J. Heldmann, D. Wooden, M. Shirley, K. Ennico, B. Hermalyn, W. Marshall, A. Ricco, R. C. Elphic, D. Goldstein, D. Summy, G. D. Bart, E. Asphaug, D. Korycansky, D. Landis, and L. Sollitt, "Detection of water in the LCROSS ejecta plume," *Science*, vol. 330, no. 6003, pp. 463–468, 2010.

[13] K. Husmann and L. Pedersen, "Strobe lit high dynamic range stereo imagery for dark navigation," in *Proc. of the 9th Int. Symp. on Artificial Intelligence for Robotics and Automation (iSAIRAS)*, Los Angeles, USA, 26–29 Feb. 2008.

[14] L. Pedersen, C. S. Han, and M. Vitus, "Dark navigation: Sensing and rover navigation in permanently shadowed lunar craters," in *Proc. of the 9th Int. Symp. on Artificial Intelligence for Robotics and Automation (iSAIRAS)*, Los Angeles, USA, 26–29 Feb. 2008.

[15] C. McManus, P. T. Furgale, and T. D. Barfoot, "Towards appearance-based methods for lidar sensors," in *Proc. of the IEEE Int. Conf. on Robotics and Automation (ICRA)*, Shanghai, China, 9–13 May 2011, pp. 1930–1935.

[16] H. J. Dong and T. D. Barfoot, "Lighting-invariant visual odometry using lidar intensity imagery and pose interpolation," in *Proc. of the Int. Conf. on Field and Service Robotics (FSR)*, Matsushima, Japan, 16–19 Jul. 2012.

[17] D. Sigel and D. Wettergreen, "Star tracker celestial localization system for a lunar rover," in *Proc. of the IEEE/RSJ Int. Conf. on Intelligent Robots and Systems (IROS)*, 29 Oct. - 2 Nov. 2007, pp. 2851–2856.

[18] N. Xiaolin and F. Jiancheng, "A new autonomous celestial navigation method for the lunar rover," *Robotics and Autonomous Systems*, vol. 57, no. 1, pp. 48 – 54, 2009.

[19] J. Enright, T. Barfoot, and M. Soto, "Star tracking for planetary rovers," in *Proc. of the IEEE Aerospace Conf.*, Mar. 2012, pp. 1–13.

[20] M. Cummins and P. Newman, "FAB-MAP: Probabilistic localization and mapping in the space of appearance," *The Int. Journal of Robotics Research*, vol. 27, no. 6, pp. 647–665, 2008.

[21] M. Shuster and S. Oh, "Three-axis attitude determination from vector observations," *Journal of Guidance and Control*, vol. 4, no. 1, pp. 70–77, 1981.

[22] M. Kaess, H. Johannsson, R. Roberts, V. Ila, J. J. Leonard, and F. Dellaert, "iSAM2: Incremental smoothing and mapping using the bayes tree," *The Int. Journal of Robotics Research (IJRR)*, vol. 31, no. 2, pp. 216–235, 2012.

[23] C. Tong and T. D. Barfoot, "Gaussian Process Gauss-Newton for 3D laser-based visual odometry," in *Proc. of the IEEE Conf. on Robotics and Automation (ICRA), to appear*, Karlsruhe, Germany, 6–10 May 2013.

BIOGRAPHY

Jonathan D. Gammell is a Ph.D. student at the University of Toronto Institute for Aerospace Studies (UTIAS), and a member of the Autonomous Space Robotics Lab (ASRL). He holds a B.A.Sc. degree (2006) from the University of Waterloo (UW) in Mechanical Engineering (Physics Option, With Distinction, Dean's Honours List), and a M.A.Sc. (2010) from the University of Toronto (UofT) in Aerospace Science and Engineering in the Space Robotics Group. His current research focus is developing planning techniques for rovers in unstructured terrain in order to minimize their final positional uncertainty.

Chi Hay Tong is a Ph.D. candidate at the University of Toronto Institute for Aerospace Studies (UTIAS), and a member of the Autonomous Space Robotics Lab (ASRL). He holds a B.A.Sc. degree (2008) from the University of Toronto (UofT) in Engineering Science (Computer Option), and his recent research focus is on laser-based mapping and navigation.

Peter Berczi is a M.A.Sc. student at the University of Toronto Institute for Aerospace Studies (UTIAS) with the Autonomous Space Robotics Lab (ASRL). He has a B.A.Sc. (Honours, 2012) from the University of Toronto (UofT) in Engineering Science (Aerospace Option). His research is focused on developing a terrain assessment framework for mobile robots, particularly for robots operating on the Moon or Mars.

Sean Anderson received a B.A.Sc. degree in Mechatronics Engineering (With Distinction, Dean's Honours List) from the University of Waterloo (UW) in 2011. Currently, he is a Ph.D. student in the Autonomous Space Robotics Lab (ASRL) at the University of Toronto Institute for Aerospace Studies (UTIAS). His main research interest is in improving Simultaneous Localization and Mapping (SLAM) algorithms for mobile robots in three-dimensional unstructured terrain.

Timothy D. Barfoot holds a B.A.Sc. (Honours, 1997) from the University of Toronto (UofT) in Engineering Science (Aerospace Option) and a Ph.D. (2002) from the University of Toronto Institute for Aerospace Studies (UTIAS) in Aerospace Engineering. He is currently an Associate Professor at UTIAS, where he leads the Autonomous Space Robotics Lab (ASRL). Before joining UTIAS, he worked at MDA Space Missions in the Controls & Analysis Group on applications of mobile robotics to space exploration and underground mining. Dr. Barfoot is a Canada Research Chair (Tier II) in Autonomous Space Robotics, a Professional Engineer of Ontario, and an IEEE Member.

John Enright holds a B.A.Sc. (1997) from the University of Toronto (UofT) (Engineering Science, Aerospace) and a M.S. (1999) and a Ph.D. (2002) from Massachusetts Institute of Technology (MIT) in Aerospace Systems. He is currently an Associate Professor in Aerospace Engineering at Ryerson University in Toronto. Having joined the faculty at Ryerson University in 2003, he is now the Principal Investigator of the Space Avionics and Instrumentation Laboratory (SAIL). While at MIT (1999-2003), he led the software development for the SPHERES flight project, and the GFLOPS real-time spacecraft simulation testbed. His research interests include spacecraft avionics and sensor processing, systems engineering and flight software. Dr. Enright is a member of the AIAA, CASI, and the IEEE.